








Particle Acceleration Controlled by Ambient Density in the Southwestern Rim of RCW 86

Hiromasa Suzuki¹ , Satoru Katsuda² , Takaaki Tanaka¹ , Nobuaki Sasaki², Tsuyoshi Inoue¹ , and Federico Fraschetti^{3,4} ¹Department of Physics, Faculty of Science and Engineering, Konan University, 8-9-1 Okamoto, Higashinada, Kobe, Hyogo 658-8501, Japan
hiromasa050701@gmail.com²Graduate School of Science and Engineering, Saitama University, 255 Shimo-Ohkubo, Sakura, Saitama 338-8570, Japan³Center for Astrophysics | Harvard & Smithsonian, Cambridge, MA 02138, USA⁴Department of Planetary Sciences, Lunar & Planetary Laboratory, University of Arizona, Tucson, AZ 85721, USA

Received 2022 March 11; revised 2022 August 28; accepted 2022 August 29; published 2022 October 13

Abstract

The physics of particle acceleration at supernova remnant (SNR) shocks is one of the most intriguing problems in astrophysics. SNR RCW 86 provides a suitable environment for understanding the physics of particle acceleration because one can extract the information on both accelerated particles and acceleration environment in the same regions through the bright X-ray emission. In this work, we study X-ray proper motions and spectral properties of the southwestern region of RCW 86. The proper motion velocities are found to be $\sim 300\text{--}2000\text{ km s}^{-1}$ at a distance of 2.8 kpc. We find two inward-moving filaments, which are more likely reflected shocks rather than reverse shocks. Based on the X-ray spectroscopy, we evaluate thermal parameters such as the ambient density and temperature, and nonthermal parameters such as the power-law flux and index. From the decrease in flux over time of several nonthermal filaments, we estimate the magnetic field amplitudes to be $\sim 30\text{--}100\text{ }\mu\text{G}$. Gathering the physical parameters, we then investigate parameter correlations. We find that the synchrotron emission from thermal-dominated filaments is correlated with the ambient density n_e as (power-law flux) $\propto n_e^{1.0\pm 0.2}$ and (power-law index) $\propto n_e^{0.38\pm 0.10}$, and not only weakly correlated with the shock velocity and shock obliquity. As an interpretation, we propose a shock–cloud interaction scenario, where locally enhanced magnetic turbulence levels have a great influence on local acceleration conditions.

Unified Astronomy Thesaurus concepts: Shocks (2086); Supernova remnants (1667); Type Ia supernovae (1728); Galactic cosmic rays (567)

1. Introduction

The physics of particle acceleration at supernova remnant (SNR) shocks is one of the principal problems in astrophysics as a promising mechanism to produce cosmic rays below the “knee” energy ($\approx 3 \times 10^{15}$ eV). X-ray and gamma-ray studies of SNRs have revealed several aspects of the physics of particle acceleration in SNRs. Völk et al. (2005) and Vink (2006) suggested that magnetic field amplification is very effective in young (<2 kyr) SNRs. High turbulence levels of magnetic fields in some parts of young SNRs were found, with the highest level close to the Bohm limit at ~ 2 kyr (Tsuji et al. 2021). Reynolds et al. (2021) studied the amount of energy in accelerated electrons and magnetic field in young SNRs based on several physical parameters such as radio luminosity, plasma density, and shock velocity, finding large variations in them among objects controlled by unknown factors. Suzuki et al. (2022) also found that the maximum energies of accelerated protons differ by more than one order of magnitude among objects at similar ages.

As the essential part of the mechanism to accelerate particles up to the knee energy, the enhancement of magnetic field strength and turbulence has been attracting particular interest (e.g., Bell 2004; Bamba et al. 2005; Vink et al. 2006; Amato & Blasi 2006; Uchiyama et al. 2007). As a possible cause of such a field enhancement, shock–cloud interactions are thought to be

important (Giacalone & Jokipii 2007; Inoue et al. 2012; Fraschetti 2013). The magnetic turbulence is expected to be amplified around dense clumps, and enhanced synchrotron X-rays have in fact been observed (e.g., Sano et al. 2013, 2015, 2017).

SNR RCW 86 provides a suitable environment for understanding the microphysics of particle acceleration. One can extract information on both the accelerated particles and acceleration environment in the same regions because the bright X-ray emission exhibits both thermal and nonthermal components. RCW 86 is believed to be the remnant of the oldest historical supernova of A.D. 185 (Stephenson & Green 2002; Green & Stephenson 2003). RCW 86 is located at $(l, b) = (315.4^\circ, -2.5^\circ)$ and has a radio shell with a radius of $\sim 21'$, which is almost completely surrounded by Balmer-dominated filaments (Smith 1997). The distance is estimated to be 2.8 kpc (Rosado et al. 1996). RCW 86 is thought to have evolved in a low-density cavity region and is currently interacting with dense materials (Williams et al. 2011). The highly irregular morphology of the SNR shell indicates that RCW 86 is currently expanding in a very inhomogeneous ambient medium. Such inhomogeneity yields a broad range of shock velocities and magnetic turbulence around the shocks that will affect the efficiency of particle acceleration. The northeastern (NE) corner is thought to be expanding in a rather low-density medium with large velocities (Yamaguchi et al. 2016) and emits hard nonthermal X-rays (Bamba et al. 2000; Vink et al. 2006). On the other hand, the radio-brightest southwestern (SW) corner is likely interacting with a dense cloud that modifies the shock structure, thereby reducing or



Original content from this work may be used under the terms of the [Creative Commons Attribution 4.0 licence](https://creativecommons.org/licenses/by/4.0/). Any further distribution of this work must maintain attribution to the author(s) and the title of the work, journal citation and DOI.

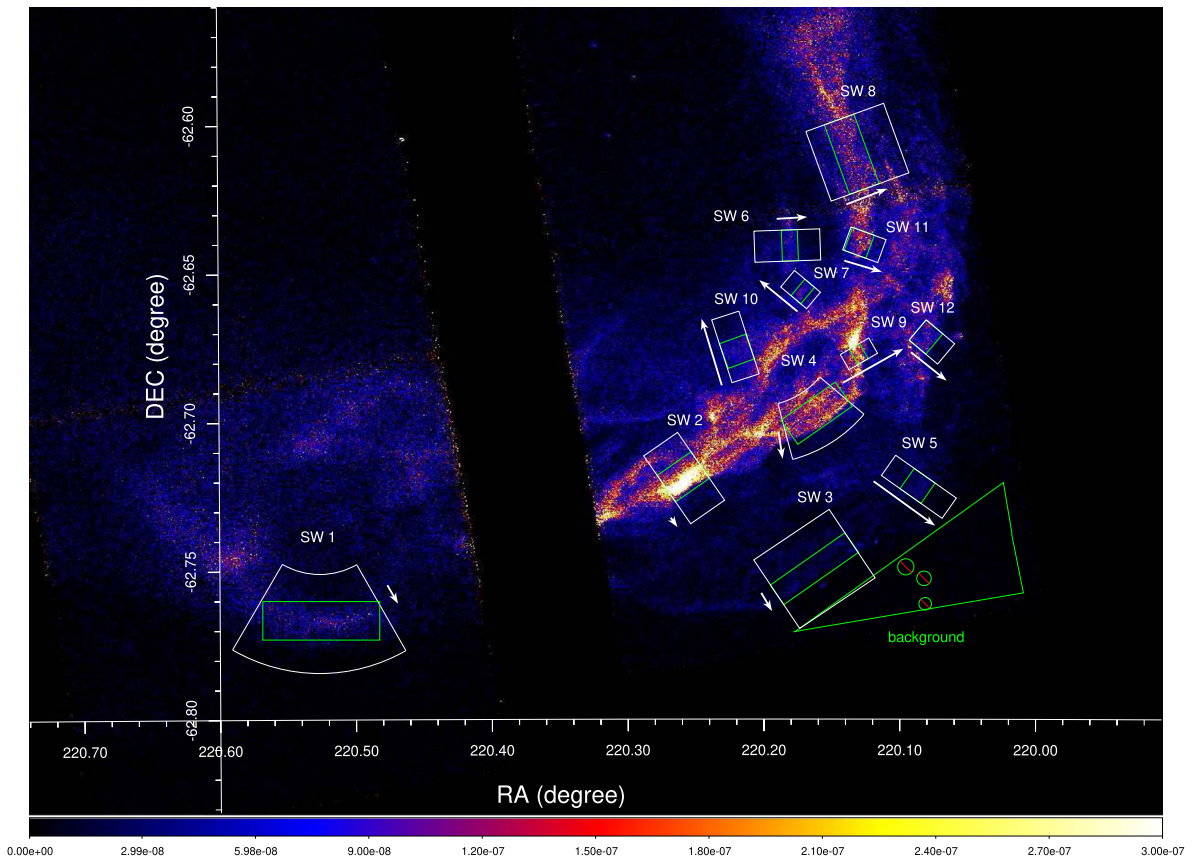


Figure 1. Exposure-corrected 0.5–7.0 keV image obtained with Chandra in 2001. The white and green lines indicate the analysis regions for proper motion and spectral studies, respectively. The arrows beside the regions indicate the filament velocities (proportional to the arrow lengths) of the filaments as described in Section 3.1.2. Their directions also correspond to the positive directions of the positions in Figures 17 and 18 in Appendix A.

Table 1
Chandra Observation Logs of the RCW 86 SW Region

OBSID	R.A. (2000)	Decl. (2000)	Roll Angle	Date	Exposure (ks)	PI
1993	220.19279	−62.66287	80°2	2001 Feb 1	92	S. Reynolds
13748	220.11392	−62.71971	70°7	2013 Feb 14	36	S. Katsuda
15610	220.11389	−62.71975	70°7	2013 Feb 17	26	S. Katsuda
15611	220.11392	−62.71971	70°7	2013 Feb 12	23	S. Katsuda

enhancing the nonthermal X-ray emission (Rho et al. 2002; Sano et al. 2017, 2019).

In this work, we focus on the SW region. We investigate the shock velocities, spectral features around shocks, and particle acceleration environments. The observation logs and data reduction process are described in Section 2. Our analysis procedure and results are presented in Section 3. The shock structures and acceleration environments are discussed in Section 4.

2. Observations and Data Reduction

We use all the four existing Chandra observations of the RCW 86 SW region listed in Table 1. The baseline for the proper motion study is ≈ 12 yr, which consists of the first-epoch observation in 2001 (OBSID 1993) and the second-epoch ones in 2013 (OBSIDs 13748, 15610, and 15611). The total exposure time is 177 ks.

The RCW 86 SW region was observed with the Advanced CCD Imaging Spectrometer (ACIS; Garmire 1997) S2, S3, and I3 in 2001 and with S2, S3, and I2 in 2013. All the data were

taken in the FAINT mode. We process the raw data following the standard data reduction method (`chandra_repro`). We used CIAO (v4.11; Fruscione et al. 2006) and calibration database 4.8.3 for the data reduction.

3. Analysis and Results

We perform proper motion study, spectroscopy, and filament-width measurement for the RCW 86 SW region. The procedures and results are presented in this section. In our analysis, we use HEASoft (v6.20; HEASARC 2014), XSPEC (v12.9.1; Arnaud 1996), and AtomDB 3.0.9. Throughout the paper, uncertainties in the text, figures, and tables indicate 1σ confidence intervals.

The wide-band (0.5–7.0 keV) and hard-band (2.0–7.0 keV) images extracted from the observation in 2001 are presented in Figures 1 and 2, respectively, with an indication of the analysis regions. Note that only SW5, SW6, SW7, SW9, and SW10 are prominent in the hard X-ray image. We also produce an image showing the difference between the exposure-corrected 1.0–5.0 keV fluxes in 2001 and 2013 (Figure 3). For some

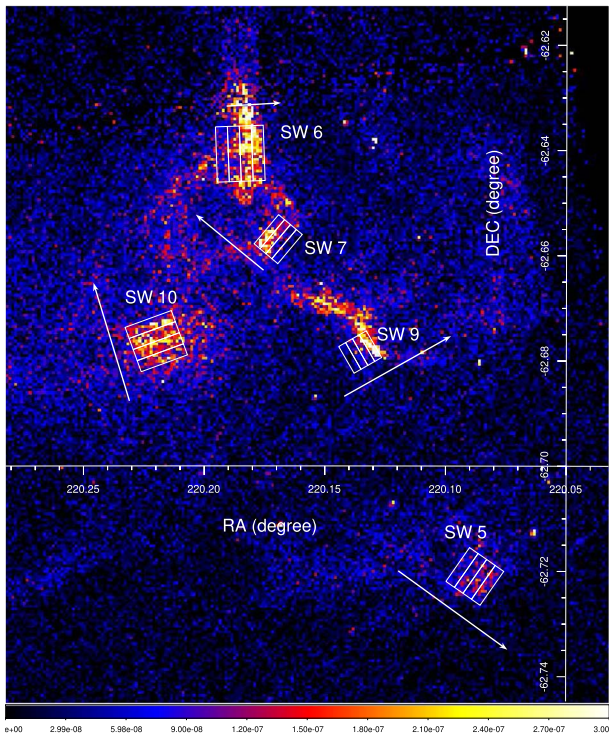


Figure 2. Exposure-corrected 2.0–7.0 keV image in 2001. The white rectangular regions are used to study the nonthermal spectral variations. The arrows beside the regions indicate the moving directions and velocities (proportional to the arrow lengths) of the filaments as described in Section 3.1.2. The arrows also correspond to the positive directions of the angular positions in Figure 9.

filaments such as SW6, SW7, and SW9, their motions are visible in this image. These 12 analysis regions are selected to enclose all the bright and sharp filament structures seen in the field of view. The directions of flux-profile extraction are defined by eye to approximately match the directions perpendicular to the filament structures.

3.1. Proper Motion Measurements

3.1.1. Aspect Correction

In order to study the proper motion with the best position accuracy available, we apply the aspect correction to the three observations in 2013. The six pointlike sources indicated in Figure 4 are selected and used for the aspect correction because they are bright and close to the nominal points in all the observations. Before the aspect correction, the positions of these sources differ among the observations by typically $\sim 0''.3$. We first run the `wavdetect` tool for each observation to determine the central positions of these sources, which are summarized in Table 2. Then we run the `wcs_match` tool to find the best-fit transformation matrices to correct the coordinate systems of the three observations in 2013 to match those of the observation in 2001.⁵ The transformation matrix only uses two-dimensional translation without rotation and scaling because the number of available pointlike sources is relatively small. Finally, the `wcs_update` tool applies these corrections to the observations in 2013.

⁵ All the six point sources are used in all the calculations without being excluded from the `wcs_match` process.

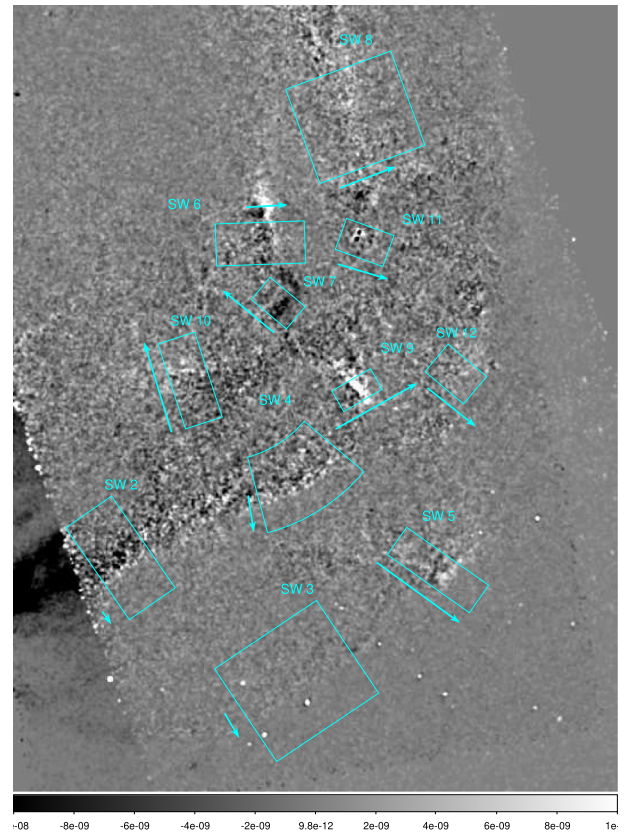


Figure 3. The image difference of the exposure-corrected 1.0–5.0 keV images between 2001 and 2013. The image is smoothed with a Gaussian kernel of $\sigma = 0''.8$. The white and black pixels show increased and decreased fluxes from 2001 to 2013, respectively. The cyan regions and arrows indicate the analysis regions and proper motion directions and velocities of the filaments. Note that a triangular region at the bottom left corner is covered only by the observation in 2001.

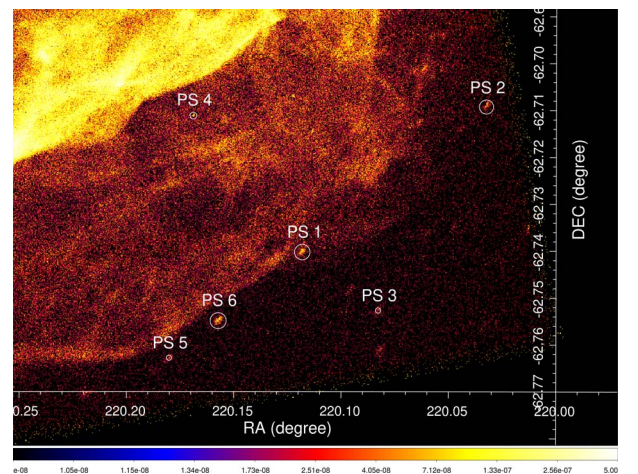


Figure 4. Exposure-corrected 0.5–7.0 keV image in 2001 with the locations of the six pointlike sources used for aspect correction indicated with white circles.

After the correction, for each of the three observations in 2013, the resultant correction accuracy is evaluated based on the standard deviation of the position offsets of the six sources with respect to those in 2001. The correction accuracies are obtained as $0''.18$, $0''.24$, and $0''.26$, for OBSIDs 13748, 15610, and 15611, respectively. We merge the three observations in 2013 for use in the following analysis. The aspect correction

Table 2
Positions of the Six Pointlike Sources

Source	Position: 1993		Diff.: 1993–15611 ^a		Diff.: 1993–13748 ^a		Diff.: 1993–15611 ^a	
	R.A. (2000)	Decl. (2000)	R.A. (arcsec)	Decl. (arcsec)	R.A. (arcsec)	Decl. (arcsec)	R.A. (arcsec)	Decl. (arcsec)
PS1	220.1181474	−62.7402549	−0.17 (0.33)	−0.04 (0.17)	−0.57 (0.29)	0.35 (0.16)	0.67 (0.43)	0.71 (0.17)
PS2	220.0325486	−62.7092583	0.29 (0.32)	−0.45 (0.10)	0.29 (0.35)	0.03 (0.10)	0.09 (0.33)	0.26 (0.10)
PS3	220.0828321	−62.7526891	−0.13 (0.26)	−0.31 (0.17)	−0.57 (0.22)	0.22 (0.18)	−0.39 (0.47)	0.46 (0.12)
PS4	220.1688151	−62.7111788	−0.26 (0.21)	−0.08 (0.12)	−0.40 (0.21)	0.45 (0.12)	−0.20 (0.21)	0.64 (0.18)
PS5	220.1801661	−62.7627948	0.64 (0.57)	−0.71 (0.26)	0.00 (0.36)	−0.24 (0.17)	0.13 (0.50)	−0.61 (0.24)
PS6	220.1572650	−62.7548930	−1.15 (0.46)	−0.44 (0.15)	−0.84 (0.32)	0.12 (0.16)	−0.62 (0.36)	−0.14 (0.21)

Note.

^a Position differences between two observations in the 0.5–7.0 keV energy range.

accuracy for these merged data is estimated to be $0''.22$ by taking an exposure-weighted average of those for the three observations, which is converted to $0''.018 \text{ yr}^{-1}$. This is considered as the systematic uncertainty associated with the position accuracy.

3.1.2. Proper Motions

Proper motion velocities of the filaments indicated in Figure 1 are measured as follows. Flux profiles are extracted from the vignetting-corrected images in 2001 and 2013, which are presented in Figures 17 and 18. To evaluate their proper motion velocities, a χ^2 test is used as below. We artificially shift the profile in 2013 by Δx and calculate $\chi^2(\Delta x)$, which is defined as

$$\chi^2(\Delta x) = \sum_i \frac{(f_i - g(\Delta x)_i)^2}{\Delta f_i^2 + \Delta g(\Delta x)_i^2}, \quad (1)$$

where f_i and Δf_i indicate the flux and error of the bin number i in 2001, and g_i and Δg_i indicate those of the shifted profile in 2013. This calculation is repeated with various values of Δx to plot χ^2 as a function of Δx . The minimum χ^2 value (χ^2_{\min}) and corresponding profile shift (Δx_{\min}) are determined by fitting the plot of χ^2 versus Δx with a parabola function. An example of the χ^2 – Δx plot and parabola fitting is presented in Figure 5. The best-fit Δx_{\min} is converted to the proper motion velocity. The profile shift is not limited to an integer multiple of the bin width. We re-bin the shifted profile $g(\Delta x)$ with the same bin arrangement as f with an assumption of a uniform probability distribution inside each bin. Then, the profile-shift ranges that give $\chi^2(\Delta x) = \chi^2_{\min} + 1$ are calculated from the best-fit parabola functions. These ranges are considered to be 1σ confidence ranges of the proper motion velocities.

The resultant proper motion estimates are summarized in Table 3 and Figure 6 and shown in Figures 17 and 18. Note that the filaments SW7 and SW10 are moving inward, toward the SNR center. These inward movements are confirmed by spectral softening toward the presumable downstream regions in SW7 and SW10 as described in Section 3.3. We also note that the projection effect, i.e., the difference between the measured radial velocities and actual three-dimensional velocities, will be small ($\lesssim 15\%$) considering the positions of the filaments with respect to the apparent SNR radius.⁶

⁶ We assume the SNR radius of $\approx 22.6'$ and radial distances of the filaments from the explosion center of ≈ 19.5 – $22.6'$.

Table 3
Proper Motion Velocities

Name	Velocity (arcsec yr ^{−1}) ^a	Velocity (km s ^{−1}) ^a
SW1	0.051 ± 0.020	660 ± 250
SW2	0.028 ± 0.005	360 ± 70
SW3	0.050 ± 0.015	650 ± 190
SW4	0.065 ± 0.007	840 ± 90
SW5	0.180 ± 0.026	2330 ± 340
SW6	0.072 ± 0.026	930 ± 340
SW7	$−0.118 \pm 0.029$	$−1530 \pm 370$
SW8	0.105 ± 0.021	1350 ± 270
SW9	0.165 ± 0.018	2130 ± 230
SW10	$−0.166 \pm 0.038$	$−2140 \pm 500$
SW11	0.093 ± 0.024	1200 ± 310
SW12	0.109 ± 0.025	1410 ± 320

Note.

^a Negative velocities indicate movements toward the SNR center.

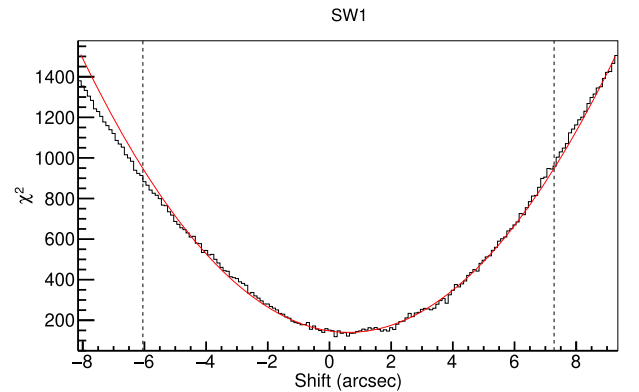


Figure 5. Example of the χ^2 test for proper motion measurement for the SW1 region. The χ^2 values (black solid line) and best-fit parabola model (red line) are shown. The black dotted lines indicate the angular range for the parabola fitting.

3.2. Filament Widths and Their Energy Dependence

In order to investigate what determines the maximum energies of accelerated electrons seen in X-rays, the filament widths and their energy dependence are measured. Here, we focus on the nonthermal-dominated filaments in 0.5–7.0 keV, SW5, SW6, SW7, and SW10. We merge the images in 2001 and 2013 and use the merged one in this section. We extract the flux radial profiles from the two energy ranges, 0.5–2.0 keV

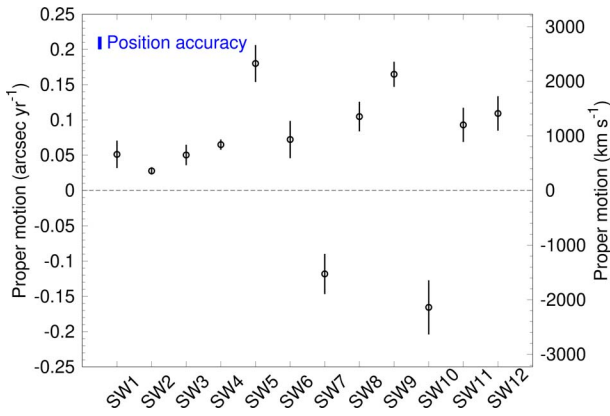


Figure 6. Proper motion estimates for individual filaments in units of arcsec yr^{-1} (on the left) and km s^{-1} (on the right). A distance of 2.8 kpc is assumed.

and 2.0–7.0 keV. To model the profiles, we use a function

$$\begin{cases} F_u(x) = C \exp\left[-\frac{x-x_0}{w_u}\right] & (x \geq x_0) \\ F_d(x) = C \exp\left[\frac{x-x_0}{w_d}\right] & (x < x_0), \end{cases} \quad (2)$$

where $F_u(x)$ and $F_d(x)$ are the presumable upstream and downstream fluxes as functions of angular position x , respectively. The parameters C , x_0 , w_u , and w_d are normalization parameter, angular position of the flux peak, and parameters to determine the widths in both regions, respectively.

The flux profiles in the soft and hard energy bands are presented in Figure 7. We fit the profile models to the data using the radial ranges where the filaments are bright compared to the background emission. We show the upstream width parameter w_u determined for the two energy ranges in the left panel of Figure 8. Based on the derived parameters, we also calculate their FWHM filament widths, which are presented in the right panel of Figure 8. Most cases show significantly narrower widths at the higher energies. Thus, their maximum energies will be determined by synchrotron cooling, as in the case of Tycho’s SNR (Tran et al. 2015) and SN 1006 (Ressler et al. 2014), not by alternative processes such as the damping of downstream magnetic field (e.g., Pohl et al. 2005), which predicts filament widths independent of photon energy.

We confirm that the energy dependence of the point-spread function (PSF) at the positions of these filaments is $\lesssim 0''.5$ by comparing the PSFs at two representative energies, 1.0 and 4.0 keV (with the tool `psfmap`; Allen et al. 2004). This small difference is because these filaments are located within $\sim 5'$ from the on-axis direction. Thus, the effect of the energy-dependent PSF on the filament widths will be negligible. Also, we check the energy dependence of the widths of the thermal-dominated filaments to examine possible systematics. We find that the widths in the 0.5–0.7 and 0.7–1.2 keV energy ranges of the thermal-dominated filaments are consistent with each other.⁷

3.3. Spectral Variations in the Downstream Regions of the Nonthermal Filaments

Here we examine the spatial variation of the spectral shapes downstream of the shocks for the nonthermal-dominated

filaments. In this section, we focus on the filaments that are nonthermal-dominated in the 1.0–7.0 keV band, SW5, SW6, SW7, SW9, and SW10.⁸ Spectral extraction regions are indicated in Figure 2. We merge the spectra in 2001 and 2013 to increase the statistics. Their proper motions are less than 30% of the widths of the extraction regions. For the spectral modeling here, we use the model, Abs.(source emission) + (sky background) + PB, where Abs. indicates interstellar absorption and PB is particle-induced background. The source emission is assumed to be powerlaw + vps shock for SW9 and powerlaw for the others. For the vps shock model, only the normalization is treated as a free parameter whereas the other parameters are fixed to the best-fit values determined in Section 3.4.2.

Resultant power-law indices are presented in Figure 9. The SW7, SW9, and SW10 regions show spectral hardening in their shock downstream regions toward the shock fronts. This is further evidence that synchrotron emission dominates the nonthermal component for these filaments (e.g., Katsuda et al. 2010; Kishishita et al. 2013). We confirm that the spectra extracted from all the regions are well explained with the powerlaw model and thus thermal contamination will be negligible.

3.4. Spectroscopy

In order to extract thermal and nonthermal properties from individual filaments, we model their energy spectra here.

3.4.1. Background Estimation

Regarding the background (sky and particle-induced background), we estimate the sky background from a region outside the SNR shell (shown in Figure 1), and model the particle-induced background using the tool `mkacispsback` (Suzuki et al. 2021). We simultaneously model the spectra extracted from the background region for both 2001 and 2013 observations. The spectral model for the background region is FE + Abs.(MWH + CXB) + PB, where FE, Abs., MWH, CXB, and PB indicate the foreground emission (Yoshino et al. 2009; Kuntz & Snowden 2000), interstellar absorption, Milky Way halo (transabsorption emission) (Masui et al. 2009; Yoshino et al. 2009; Kuntz & Snowden 2000), cosmic X-ray background (Snowden et al. 1992; Kushino et al. 2002; Hickox & Markevitch 2006), and particle-induced background model suited for our background region.

The FE component is described by the `apec` model with the fixed temperature of 0.1 keV and metal abundances of solar values. The emission measure, which is defined as $10^{-10}(4\pi D^2)^{-1} \int n_e n_H dV$ (in cm^{-5}), where D , n_e , and n_H stand for distance and electron and hydrogen number densities, respectively, is treated as a free parameter. The absorption column density of the Abs. component (`tbabs` model) is fixed to $N_H = 6.4 \times 10^{21} \text{ cm}^{-2}$ (HI4PI Collaboration et al. 2016). The MWH component is also described with the `apec` model with fixed metal abundances of solar values and free temperature and emission measure. The CXB component is described by the `powerlaw` model with a fixed spectral index of 1.4 and the normalization corresponding to a flux of $6.38 \times 10^{-8} \text{ erg cm}^{-2} \text{ s}^{-1} \text{ sr}^{-1}$ (Kushino et al. 2002). As for the particle-induced background, the `acispsback` model predicts a lower flux than the observation in the $\sim 2\text{--}7$ keV band only in 2001 (Suzuki et al. 2021). Thus, we apply an additional `powerlaw` model to `acispsback` only for the spectra in 2001.

⁷ For SW1, as an example, the FWHM filament widths in the lower and higher energy ranges are $42 \pm 6''$ and $49 \pm 3''$, respectively.

⁸ We find that the nonthermal parameters are constrained well if a spectrum is nonthermal-dominated above ~ 1 keV.

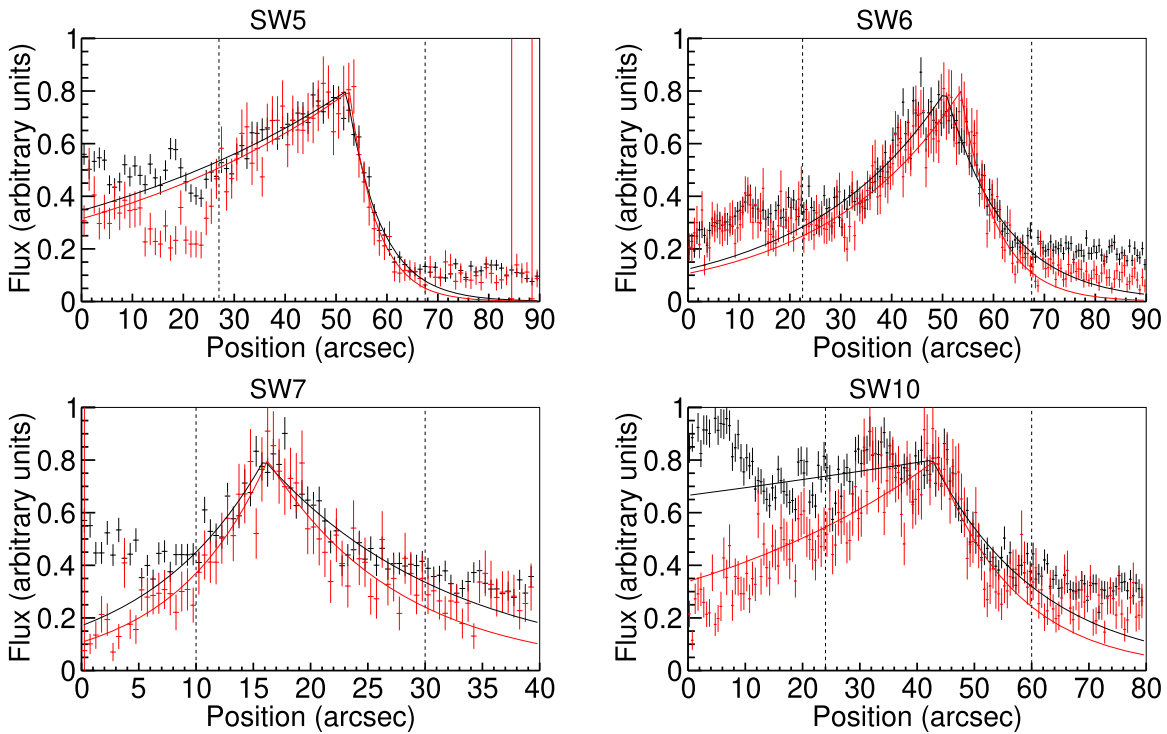


Figure 7. Flux profiles of the nonthermal filaments. The extraction energy ranges are 0.5–2.0 keV (black) and 2.0–7.0 keV (red). Increasing positions correspond to the directions of the arrows shown in Figure 1. The displayed flux ranges are different for different panels. The best-fit models for the two profiles are overlapped with black and red solid lines, respectively. Radial ranges used for the fitting are indicated with black dotted lines.

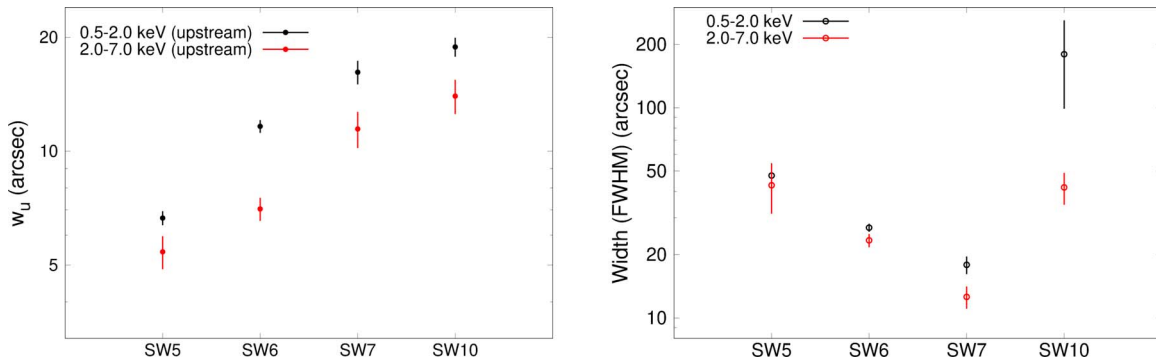


Figure 8. Upstream width parameter w_u and FWHM filament widths of the nonthermal filaments in the 0.5–2.0 keV and 2.0–7.0 keV energy ranges.

The spectral fitting results are shown in Figure 10. The best-fit spectral parameters are summarized in Table 4. The spectral parameters are consistent with Kuntz & Snowden (2000) and Yoshino et al. (2009). Note that the decrease in visible flux from 2001 to 2013 at the energies below 1 keV is due to the increased contamination on the sensor surface.

3.4.2. Spectral Modeling for Filaments

As the source emission, we apply the `vpshock` (nonequilibrium ionizing plasma) model to the thermal component, and the `powerlaw` model to the nonthermal component following Tsubone et al. (2017). In addition, a Gaussian with a fixed energy centroid of 6.4 keV and width of zero is added for all the regions (Yamaguchi et al. 2011; Tsubone et al. 2017). The spectral model is described as `Abs.(source emission) + (sky background) + PB`. The source emission is `powerlaw` for SW5, SW6, SW7, and SW10 because thermal components are found to be unnecessary. The model `vpshock + powerlaw` is applied for the other regions. We note

that the regions SW9 and SW12 are intermediate cases between the nonthermal- and thermal-dominated ones. The absorption column density of the `Abs.` component (`tbabs` model) is treated as a free parameter. For `vpshock`, the temperature, ionization timescale ($n_e t$), emission measure, and the metal abundances of O, Ne, Mg, Si, and S are treated as free parameters. The other metal abundances are fixed to solar values. All the parameters of `vpshock` are tied between 2001 and 2013. The `powerlaw` normalization and index are treated as free parameters and are basically tied between 2001 and 2013. Only for SW5, SW6, SW7, and SW10 are both parameters untied between 2001 and 2013. The sky background component is the same as that determined in Section 3.4.1. The overall normalization of all the parameters are scaled by the area ratio between the source regions and background region. The PB component for the spectra in 2001 is composed of `acipback` plus `powerlaw` models, whereas that for 2013 is a simple `acispback` model, which is the same treatment as that for the background estimation.

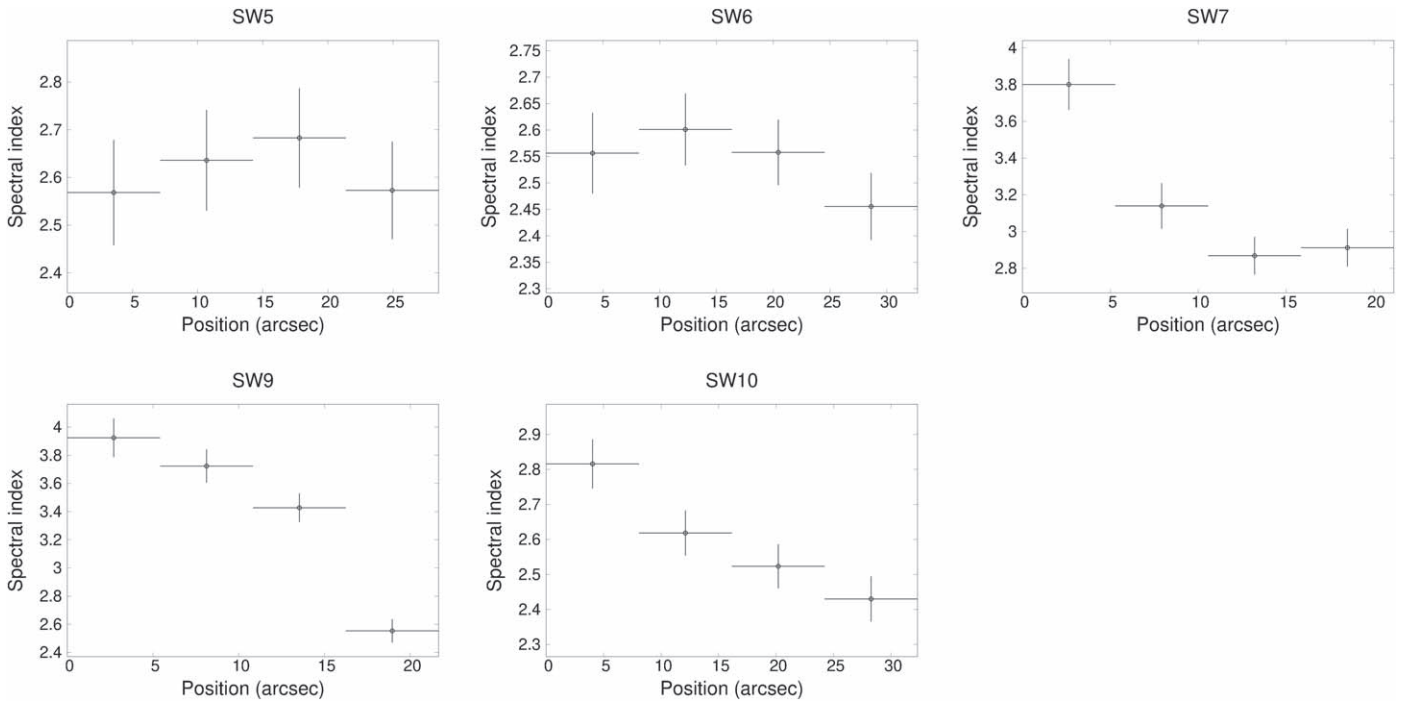


Figure 9. Variation of power-law indices in the downstream regions toward the filaments for SW5, SW6, SW7, SW9, and SW10. Increasing positions correspond to the directions of the arrows beside the regions in Figure 2. For each panel, the cross with the largest position is the data at the filament.

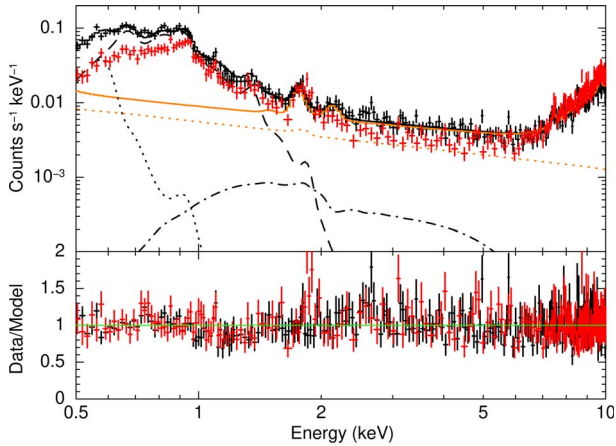


Figure 10. Energy spectra and best-fit models for the background region. The black and red crosses represent the data in 2001 and 2013, respectively. The model spectra only for the data in 2001 are overlotted with lines. The black solid line represents the entire model. The black dotted, dashed, and dashed-dotted lines show the FE, MWH, and CXB spectral models, respectively. The orange dotted and solid lines represent the additional powerlaw model to the PB component and the entire PB spectral model, respectively.

The spectra and best-fit models are presented in Figure 11. The resultant spectral parameters are summarized in Table 5. The power-law fluxes of SW5, SW6, SW7, and SW10 all show significant decreases from 2001 to 2013. Similarly, the power-law indices increase (spectra soften) from 2001 to 2013. The absorption column densities, temperatures, metal abundances, and ionization timescales are roughly consistent with those presented in Tsubone et al. (2017). From the plasma densities inferred from the emission measures ($\sim 1 \text{ cm}^{-3}$) and ionization timescales ($(5\text{--}13) \times 10^{10} \text{ s cm}^{-3}$), we confirm⁹ that the elapsed

⁹ With an assumption that our analysis regions are cuboids.

Table 4
Best-fit Spectral Parameters for the Background Region

Model	Parameter	Value
Abs.	N_{H} (10^{22} cm^{-2})	0.64 (fixed)
FE	kT (keV)	0.1 (fixed)
	Abundance (solar)	1 (fixed)
	EM ^a	$(9.7 \pm 1.2) \times 10^{-1}$
MWH	kT (keV)	0.18 ± 0.03
	Abundance (solar)	1 (fixed)
	EM ^a	4.5 ± 0.3
CXB	Photon index	1.4 (fixed)
	Normalization ^b	4.32×10^{-6} (fixed)

Notes.

^a Emission measure, $10^{-10}(4\pi D^2)^{-1} \int n_e n_H dV$ (in cm^{-5}), where D , n_e , and n_H stand for distance (cm) and electron and hydrogen number densities (cm^{-3}), respectively.

^b Normalization of the power-law model in units of $\text{cm}^{-2} \text{ s}^{-1} \text{ keV}^{-1}$ at 1 keV.

times after the shock heating are comparable to the remnant age ($\sim 2000 \text{ yr}$). The SW3 region may show a shorter elapsed time of $\sim 600 \text{ yr}$. This is consistent with the fact that this region is more distant from the remnant center than the other filaments and will be less affected by the projection effect, which mixes the newly heated and older regions. We also search for possible variations of the nonthermal parameters in the thermal-dominated cases where the spectral model fits the data relatively well (e.g., SW9 and SW12), and find consistent parameters in 2001 and 2013.¹⁰

We also use the spectral model by Zirakashvili & Aharonian (2007; hereafter the ZA07 model) for the nonthermal component to discuss the acceleration efficiency. The ZA07 model is described as

¹⁰ For example, the power-law fluxes of SW9 in the 0.5–7.0 keV band in 2001 and 2013 are $3.6\text{--}4.5 \times 10^{-13} \text{ erg}$ and $4.4\text{--}5.5 \times 10^{-13} \text{ erg}$, respectively.

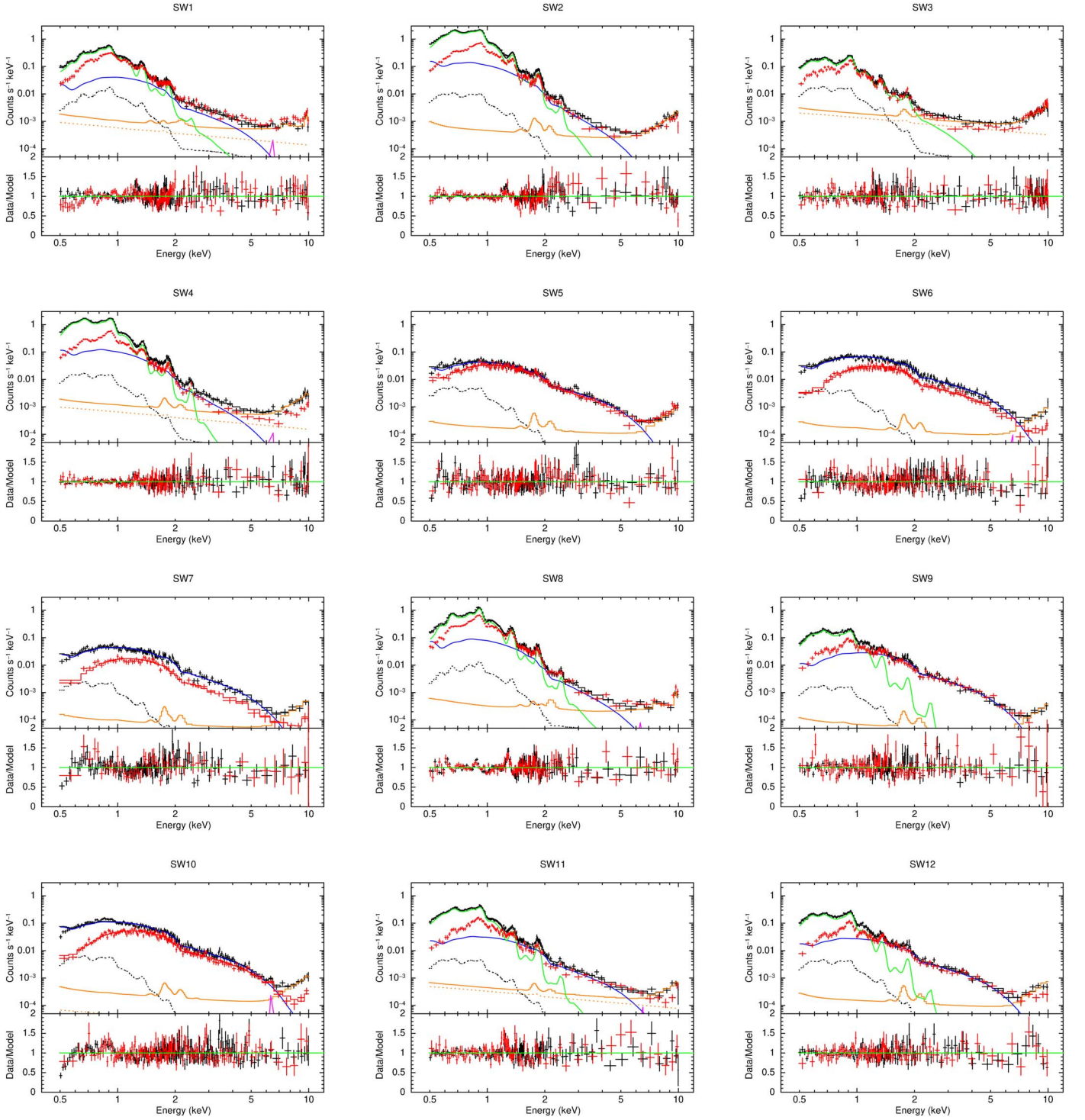


Figure 11. Spectral modeling results for individual filaments. Black and red crosses are the observations in 2001 and 2013, respectively. In each panel, the upper and lower parts show the flux and data-to-model ratio, respectively. The best-fit model spectra only for the data in 2001 are overlotted with lines. The black solid lines represent the entire models. The green, blue, and magenta solid lines represent the thermal (`vpshock`), nonthermal (`powerlaw`), and Gaussian components, respectively. The orange dotted and solid lines show the additional `powerlaw` models to the PB component and the entire PB models, respectively. The black dotted lines show the sky background components.

$$\frac{dN}{dE} \propto \left(\frac{E}{E_0}\right)^{-2} \left[1 + 0.38\left(\frac{E}{E_0}\right)^{1/2}\right]^{11/4} \times \exp\left[-\left(\frac{E}{E_0}\right)^{1/2}\right], \quad (3)$$

where E and E_0 indicate photon energy and spectral turnover energy, respectively. This model describes the synchrotron emission spectrum with several assumptions: loss-limited maximum energy, arbitrary energy dependence of the diffusion coefficient, shock compression ratio of four, and upstream-to-downstream magnetic field ratio of $\sqrt{11}$. We replace the `powerlaw` model in the spectral

Table 5
Best-fit Spectral-model Parameters for the Filament Regions

Name	Abs. N_{H} (10^{22} cm $^{-2}$)	powerlaw		vpshock							Gaussian Norm. ^c	C-stat (d.o.f.)
		$\log_{10}(\text{Flux (erg cm}^{-2} \text{ s}^{-1}))^{\text{a}}$	Photon Index	kT (keV)	$n_{\text{e}f}$ (10^{10} cm $^{-3}$ s $^{-1}$)	EM ^b	O (solar)	Ne (solar)	Mg (solar)	Si (solar)		
SW1	0.23 ± 0.02	-12.21 ± 0.02	3.14 ± 0.12	0.60 ± 0.04	4.9 ± 0.9	6.9 ± 1.0	0.74 ± 0.05	1.43 ± 0.09	1.31 ± 0.09	1.26 ± 0.14	9.3 ± 4.5	1603.64 (1288)
SW2	0.34 ± 0.02	-11.89 ± 0.02	4.31 ± 0.12	0.41 ± 0.02	12.5 ± 1.5	25.8 ± 2.9	1.02 ± 0.04	2.11 ± 0.07	1.44 ± 0.06	1.62 ± 0.09	2.4 ± 2.0	1798.70 (1288)
SW3	0.44 ± 0.02	0.72 ± 0.07	0.97 ± 0.05	4.2 ± 0.9	0.78 ± 0.07	1.23 ± 0.10	0.79 ± 0.09	1.00 ± 0.22	<3.5	1373.35 (1290)
SW4	0.43 ± 0.02	-11.89 ± 0.02	4.18 ± 0.12	0.38 ± 0.02	7.7 ± 1.0	25.2 ± 4.4	1.59 ± 0.08	2.49 ± 0.12	1.45 ± 0.08	2.28 ± 0.16	3.3 ± 2.3	1468.98 (1287)
SW5	0.26 ± 0.01	-12.32 ± 0.01 (-12.34 ± 0.01)	2.59 ± 0.07 (2.81 ± 0.06)	1.2 ± 1.5	1405.35 (1293)
SW6	0.33 ± 0.01	-12.04 ± 0.01 (-12.10 ± 0.01)	2.46 ± 0.05 (2.66 ± 0.05)	2.4 ± 2.1	1315.36 (1293)
SW7	0.32 ± 0.02	-12.28 ± 0.01 (-12.38 ± 0.01)	2.82 ± 0.08 (3.23 ± 0.08)	<1.8	1231.83 (1293)
SW8	0.27 ± 0.01	-12.00 ± 0.02	4.10 ± 0.11	0.55 ± 0.02	7.7 ± 0.09	9.15 ± 0.07	1.15 ± 0.06	2.35 ± 0.09	1.54 ± 0.07	1.51 ± 0.11	2.7 ± 1.8	1799.19 (1287)
SW9	0.40 ± 0.06	-12.34 ± 0.01	2.66 ± 0.08	0.36 ± 0.02	9.5 ± 3.6	2.6 ± 1.1	1.52 ± 0.18	2.67 ± 0.41	1.85 ± 0.36	1.90 ± 0.86	1.4 ± 1.2	1211.74 (1288)
SW10	0.25 ± 0.01	-11.93 ± 0.01 (-11.97 ± 0.01)	2.57 ± 0.05 (2.69 ± 0.04)	4.9 ± 2.5	1468.25 (1293)
SW11	0.33 ± 0.03	-12.52 ± 0.02	2.98 ± 0.12	0.50 ± 0.04	7.3 ± 1.7	3.0 ± 0.6	1.00 ± 0.08	2.16 ± 0.16	1.36 ± 0.13	1.95 ± 0.25	3.9 ± 1.7	1336.28 (1287)
SW12	0.28 ± 0.05	-12.49 ± 0.02	2.57 ± 0.09	0.46 ± 0.05	4.5 ± 1.2	1.7 ± 0.7	1.01 ± 0.09	2.49 ± 0.39	1.43 ± 0.26	2.18 ± 0.66	<2.0	1316.22 (1288)

Notes.

^a Unabsorbed flux in the 0.5–7.0 keV energy range. For those with two values, the values in 2001 (2013) are shown.

^b Emission measure in the same units as that in Table 4.

^c Total flux of the Gaussian model in units of 10^{-7} photons cm $^{-2}$ s $^{-1}$. The energy centroid of the Gaussian component is fixed to 6.4 keV.

Table 6
Best-fit Parameters of the **ZA07** Model

Name	E_0 (keV) ^a
SW1	0.18 ± 0.03
SW2	0.041 ± 0.004
SW3	...
SW4	0.051 ± 0.005
SW5	0.42 ± 0.06 (0.24 ± 0.02)
SW6	2.35 ± 0.76 (1.92 ± 0.64)
SW7	0.26 ± 0.03 (0.13 ± 0.01)
SW8	0.08 ± 0.01
SW9	1.72 ± 0.72
SW10	0.45 ± 0.04 (0.33 ± 0.02)
SW11	0.24 ± 0.05
SW12	2.52 ± 1.69

Note.

^a Values are tied between the data in 2001 and 2013 except for those for SW5, SW6, SW7, and SW10, for which the values in 2001 (2013) are shown.

model set used above with the **ZA07** model. The free parameters for spectral modeling are the same as those in the case with the powerlaw model except for the normalization and turnover E_0 of the **ZA07** model. The results are summarized in Table 6. One can see that the nonthermal-dominated filaments, SW5, SW6, SW7, and SW10, exhibit decreasing E_0 over time, which is the same tendency as our results with the powerlaw model.

4. Discussion

4.1. Magnetic Field Amplitude

We have found that the nonthermal-dominated filaments SW5, SW6, SW7, and SW10 showed a decrease in flux from 2001 to 2013. This is seen in Figure 12. The decrease rates are from $\sim 0.4\% \text{ yr}^{-1}$ (SW5) to $\sim 2\% \text{ yr}^{-1}$ (SW7). Given that the nonthermal emissions are dominated by synchrotron radiation, it is reasonable to attribute such decreases in flux to synchrotron cooling. The cooling timescale is described as

$$t_{\text{syn}} = 50 \text{ yr} \times \left(\frac{E}{1 \text{ keV}} \right)^{-0.5} \left(\frac{B}{100 \mu\text{G}} \right)^{-1.5}, \quad (4)$$

where E and B represent the synchrotron photon energy and magnetic field strength, respectively. Thus, the decreases in flux roughly require field strengths of $\sim 30\text{--}100 \mu\text{G}$. Such field strengths are similar to the previous estimates ($24 \mu\text{G}$ by Vink et al. (2006) based on filament widths; $35 \mu\text{G}$ by Helder et al. (2012) based on filament widths; $14\text{--}20 \mu\text{G}$ by Yuan et al. (2014) based on the broadband spectrum).

The magnetic field strength at a filament can also be estimated based on the filament width seen in X-rays. As presented in Vink et al. (2006), the magnetic field strength is simply determined by the filament width w at the target distance d as

$$B = 54 \mu\text{G} \times (w/0.1 \text{ pc})^{-2/3} \\ \approx 54 \mu\text{G} \times (w/7.3'')^{-2/3} (d/2.8 \text{ kpc})^{-2/3}, \quad (5)$$

if the energy range for the width estimation is near the roll-off energy of the synchrotron emission. We thus obtain magnetic field strengths of $\sim 20\text{--}50 \mu\text{G}$ for SW5, SW6, SW7, and SW10 based on Figure 8. These estimates are also consistent with the

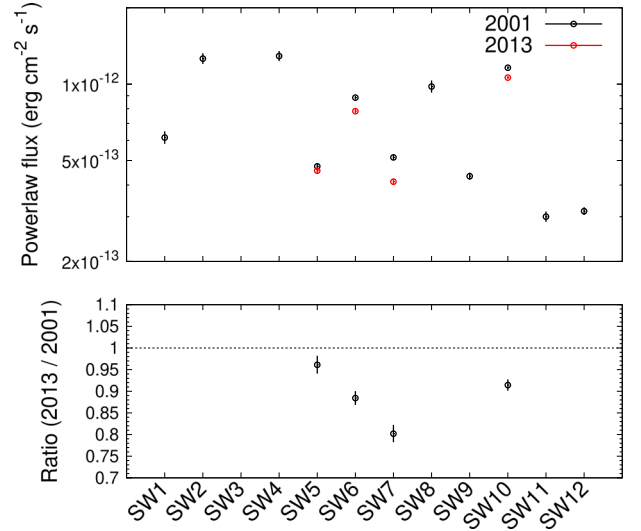


Figure 12. Power-law fluxes of the individual filaments (top) and their 2013-to-2001 ratios (bottom; only for the nonthermal-dominated filaments). The flux is calculated for the 0.5–7.0 keV energy range.

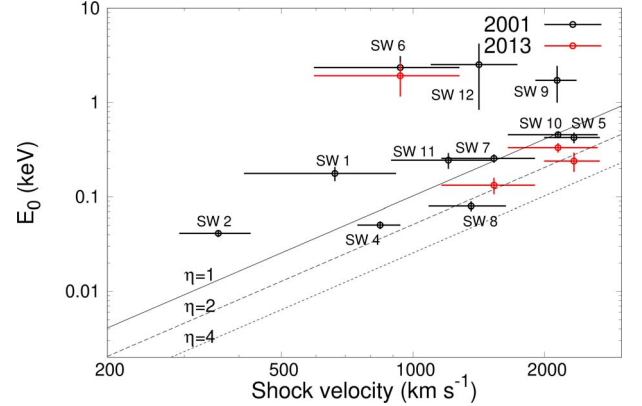


Figure 13. Plots of the cutoff energy of the **ZA07** model (E_0) against the shock velocity (proper motion velocity is substituted). A distance of 2.8 kpc is assumed. The black solid, dashed, and dotted lines indicate the **ZA07** model with different gyrofactors (η).

previous estimates (Vink et al. 2006; Helder et al. 2012; Yuan et al. 2014).

4.2. Magnetic Field Turbulence Level

Based on the shock velocity (v_{sh}) and turnover energy of the **ZA07** model (E_0), one can estimate the gyrofactor ($\eta = (B/\delta B)^2$, where B and δB are the magnetic field amplitude and fluctuation, respectively). Zirakashvili & Aharonian (2007) derived E_0 as a function of η and v_{sh} as

$$E_0 = 0.24 \text{ keV} \times \eta^{-1} (v_{\text{sh}}/2000 \text{ km s}^{-1})^2. \quad (6)$$

Figure 13 exhibits the plots of E_0 against the shock velocity, for which the proper motion velocity is simply substituted. Compared to the “ $\eta = \text{const.}$ ” lines, SW3, SW4, SW5, SW7, SW8, SW10, SW11, and SW12 are consistent with $\eta = 1\text{--}4$, whereas SW1, SW2, SW6, and SW9 have $\eta < 1$. Such small values of η indicate the existence of highly amplified magnetic turbulence. This is similar to the situations of SN 1006 (Ressler et al. 2014) and RX J1713.7–3946 (Tsuji et al. 2019).

Dickel et al. (2001) found a low degree of polarization in the RCW 86 SW region and proposed a Faraday depolarization scenario. The high level of magnetic turbulence suggested by our results can be an alternative to this low degree of polarization.

Given that RCW 86 is thought to have begun to interact with the cavity wall recently (Williams et al. 2011), such small η values might indicate that the shocks have been decelerated just recently, whereas the accelerated particles remain as they were before the interaction. This would be reasonable if the synchrotron cooling timescales we evaluated ($\gtrsim 50$ – 200 yr) are longer than the deceleration timescales of the shocks. We basically believe that the projection effect on the proper motions will be small ($\lesssim 15\%$; see Section 3.1.2), but it still possibly contributes to such small η values because of the complicated shock structure. It is also possible that these small η values are due to the uncertainties in the distance to RCW 86. A distance a factor of two larger would result in $\eta \gtrsim 1$ for most of the filaments. Note that larger distances, on the other hand, would put the magnetic field estimates based on the filament widths in tension with those from the decrease in flux (Section 4.1).

4.3. Nature of the Inward-moving Filaments

We have found that the SW7 and SW10 filaments are moving inward. The spectral softening toward the downstream regions is also confirmed (Section 3.3), which supports their inward movements. Here we discuss their nature: reverse or reflected shocks.

Assuming that they are reverse shocks, we can estimate their shock velocities in the unshocked-ejecta frame by assuming coordinates for the explosion center. The explosion center is substituted with the geometrical center, and is assumed to be $(l, b) = (315^\circ 40' 68'', -2^\circ 31' 51'')$ by fitting the radio shell with a circle by eye. The ejecta velocities in the laboratory frame (v_{ej}) and the estimated shock velocities (v_{rev}) are summarized in Table 7. These velocities would be too large considering their values of E_0 , i.e., they would require much larger values of the gyrofactor η than the other filaments (Figure 13). Given that SW7 and SW10 are associated with rather hard X-ray emission, it would be unreasonable if they were outliers in Figure 13 with particularly large η values.¹¹ Besides, the presumable reverse-shock velocities of $\sim 10,000$ km s⁻¹ are even larger than the shock velocities inferred for the inward-moving filaments observed in Cassiopeia A (e.g., Sato et al. 2018).

On the other hand, if we assume that the inward-moving filaments are reflected shocks, we cannot simply estimate their shock velocities without certain assumptions (e.g., Truelove & McKee 1999). In this case, the reflected shocks should be moving in the shocked ejecta. If the ejecta were decelerated significantly (e.g., by the cavity wall as suggested by Williams et al. (2011) or dense clouds as suggested by Sano et al. (2019)), the shock velocities with respect to the shocked ejecta would be as small as those of the other filaments (Figure 13). Thus, we propose the reflected-shock scenario as the most likely nature of the two inward-moving filaments.

4.4. Maximum Energies of Accelerated Protons

As we have obtained several parameters related to particle acceleration, the age t , shock velocity v_{sh} , magnetic field strength B , and gyrofactor η , we derive here the maximum energies of particles. Those of protons are of particular interest.

¹¹ Note that the large η values of ~ 20 suggested in the reverse-shock scenario for SW7 and SW10 are not unreasonable themselves, because similar values of η have been found in other SNRs with similar ages (Tsuji et al. 2021).

Table 7
Shock Velocities in the Reverse Shock Scenario

Name	Radius (arcmin) ^a	v_{ej} (km s ⁻¹) ^b	v_{rev} (km s ⁻¹) ^c
SW5	22.8826	9668	7300 ± 700
SW6	17.6610	7462	6500 ± 700
SW7	18.4815	7809	9300 ± 900
SW10	18.1032	7649	9800 ± 1000

Notes.

^a Filament position with respect to the geometrical center $(l, b) = (315^\circ 40' 68'', -2^\circ 31' 51'')$.

^b Fast-moving ejecta velocity in the laboratory frame.

^c Shock velocity in the ejecta frame.

With an assumption that the maximum proton energy ($E_{max,p}$) is limited by the acceleration time and that the diffusion coefficient is time-invariant, $E_{max,p}$ can be written as (e.g., Reynolds 2008; Yamazaki et al. 2014)

$$E_{max,p} \approx 200 \text{ TeV } \eta^{-1} \times \left(\frac{v_{sh}}{2000 \text{ km s}^{-1}} \right)^2 \left(\frac{B}{50 \mu\text{G}} \right) \left(\frac{t}{2 \text{ kyr}} \right). \quad (7)$$

If we substitute the parameters for SW7, $\eta \approx 1$, $v_{sh} \approx 1600$ km s⁻¹, and $B \sim 100 \mu\text{G}$ (based on the nonthermal decrease in flux), we obtain $E_{max,p} \sim 210$ TeV. Similarly, for SW5, SW6, and SW10, we obtain $E_{max,p} \sim 140$, 130, and 240 TeV, respectively. These estimates are consistent with the maximum energies evaluated from the gamma-ray spectrum assuming hadronic gamma rays, ≈ 10 – 200 TeV (Yuan et al. 2014; Zeng et al. 2019; Suzuki et al. 2020, 2022).¹² Thus, our parameter estimates such as the magnetic field strength and turbulence level would be reasonable.

4.5. Acceleration Parameters and Their Dependence on Environment

4.5.1. Parameter Correlations

Based on the proper motions and spectral parameters we have obtained, we discuss here the correlations of these parameters to see how the environmental parameters affect the acceleration processes. Figure 14 shows the power-law parameters versus shock velocity, thermal emission measure, and electron temperature. Focusing on the filaments with both thermal and nonthermal parameters obtained (black crosses), the power-law parameters clearly depend on the emission measure ($\propto n_e^2 V$, where n_e and V are plasma density and volume, respectively) and do not or only weakly depend on the shock velocity and post-shock electron temperature. If we evaluate the correlation between the downstream plasma density and power-law parameters with a power-law function, we obtain (power-law flux) $\propto n_e^{1.0 \pm 0.2}$ and (power-law index) $\propto n_e^{0.38 \pm 0.10}$. Note that the nonthermal-dominated filaments, SW5, SW6, SW7, and SW10, are not included in these evaluations. Such correlations were indeed implied by Tsubone et al. (2017) using Suzaku by investigating the whole remnant, but are more clarified in this work with Chandra. An increase in the nonthermal flux associated with high-density regions was also observed in Cassiopeia A (Sato et al. 2018; Fraschetti et al. 2018).

¹² We note that our estimates are also consistent with the leptonic scenario, where the proton maximum energy of $\gtrsim 20$ TeV is indicated.

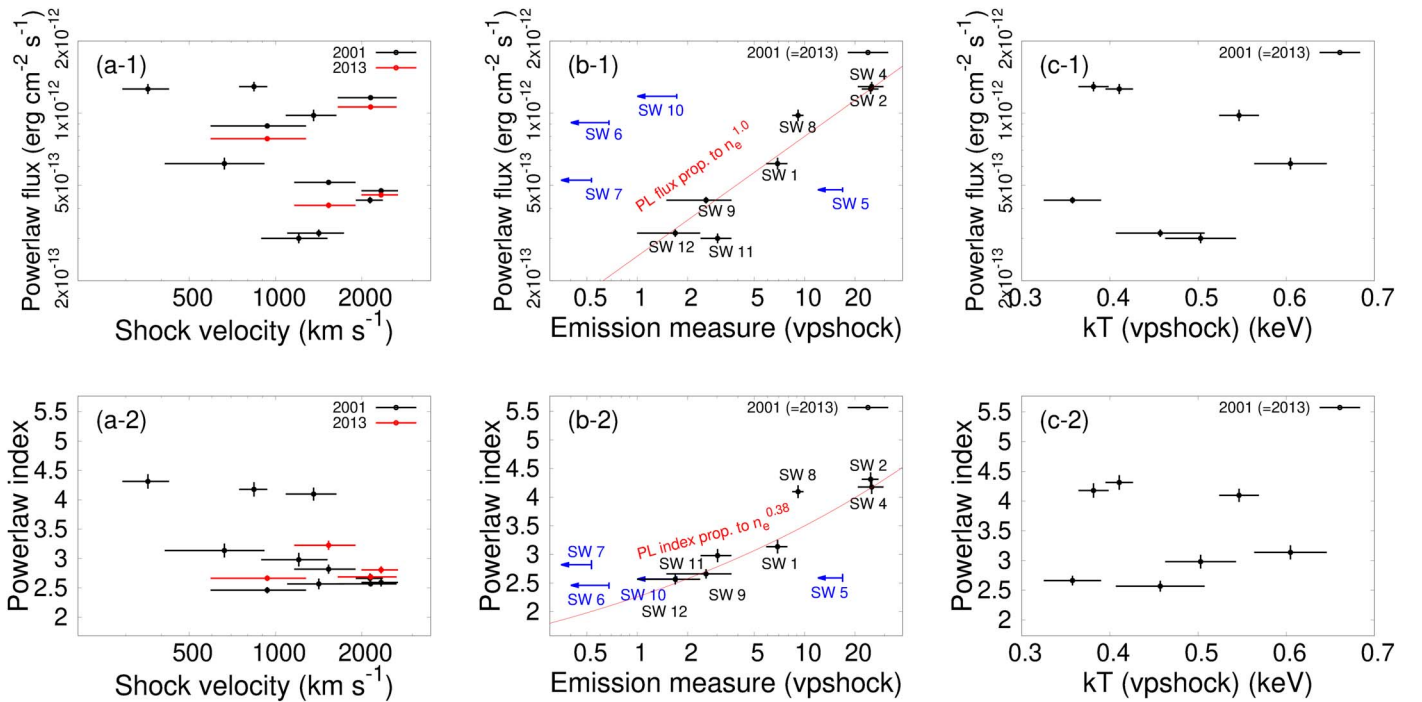


Figure 14. Plots of the power-law (PL) flux and index as functions of the shock velocity (proper motion velocity is substituted), emission measure ($\propto n_e^2$), and electron temperature (kT). The PL flux is calculated for 0.5–7.0 keV. The EM is shown in the same units as in Table 4. The 95% upper limits of the EMs of the nonthermal-dominated filaments are shown with the blue arrows in panels (b). The best-fit power-law functions for the plots of the PL flux and index over the emission measure are also shown with red lines.

As seen in Figure 15, the emission measure is negatively correlated with the shock velocity v_{sh} . This correlation appears to follow the function $n_e v_{\text{sh}} = \text{const}$. A simple assumption of constant ram pressure $n_e v_{\text{sh}}^2 = \text{const}$ seems to be inapplicable. This may reflect the inhomogeneity in the ambient density suggested by the complicated structure of the remnant and discussed in previous works (Williams et al. 2011; Tsubone et al. 2017). We note that additional uncertainties of the shock velocity are expected in the direction of motion and the projection effect, which would be less than a factor of about two.

Certain correlations among magnetic field strength B , density n_e , and shock velocity v_{sh} are expected due to the Bell instability (Bell 2004), and were in fact confirmed from observations of several young SNRs (Völk et al. 2005; Vink 2006, 2017; Helder et al. 2012): $B^2 \propto n_e v_{\text{sh}}^3$ or $B^2 \propto n_e v_{\text{sh}}^2$. If we plot the filament width ($\propto B^{-3/2}$ by Equation (5)) over the shock velocity for SW5, SW6, SW7, and SW10, we obtain Figure 16. As can be seen, the data do not follow the relations expected above.

In order to compare the parameter correlations of the nonthermal-dominated filaments to those of the thermal-dominated ones, we evaluate the upper limits of the EMs for the nonthermal-dominated filaments (SW5, SW6, SW7, SW9, and SW10). We repeat the spectral modeling described in Section 3.4.2 with an additional ionizing plasma model with various electron temperatures (0.3–0.8 keV) and ionization timescales (10^{10-11} s cm^{-3}) with the metal abundances fixed to solar, and derive the upper limit of the EM.¹³ The resulting upper limits of the EMs versus the power-law parameters are shown in Figure 14(b). The nonthermal-dominated filaments located in the inner regions, SW6, SW7, and SW10, do not

follow the same tendency as that of the other filaments (shown with the red solid lines).

We have also investigated the dependence of the nonthermal parameters on the shock obliquity (angle between the shock normal and background magnetic field). The background field direction is estimated from the polarization of starlight at similar distances to RCW 86 (see Appendix B for more details). The field direction around RCW 86 is found to be nearly parallel to the Galactic plane. We find no correlation between the nonthermal parameters and the shock obliquity, as can be seen in Figure 20.

4.5.2. Scenario to Explain the Measurements: Shock–Cloud Interaction

We propose here a shock–cloud interaction scenario to explain the parameter correlations we have obtained above. The RCW 86 SW region is interacting with dense atomic and molecular clouds (Sano et al. 2017, 2019), X-ray emission is expected to trace such an interaction. The shock–cloud interaction will slow down the shocks and will damp the magnetic turbulence inside dense clumps but amplify the magnetic turbulence around them (Inoue et al. 2012; Frascchetti 2013). If our analysis has resolved such clumpy structures, we expect harder synchrotron X-rays for lower-density regions due to higher maximum acceleration energies, which matches the measured trend (Figure 14(b)). We note that our spectral extraction regions have a size of ~ 0.2 – 0.4 pc at a distance of 2.8 kpc, and the shock crossing time is estimated as ~ 100 – 1000 yr. Since the cooling timescale derived for the nonthermal-dominated filaments of ~ 50 – 200 yr is similar to the shock crossing timescale, it will be reasonable to assume that the spatial extents of clumps are similar to our region sizes. The fact that the power-law flux is proportional to the density

¹³ The two parameter ranges are selected based on the values determined for the thermal-dominated filaments (Table 5).

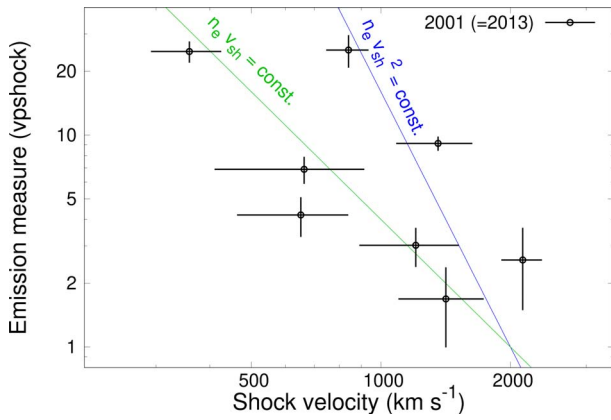


Figure 15. Plots of the emission measure ($\propto n_e^2$) as a function of the shock velocity (v_{sh} ; proper motion velocity is substituted). A distance of 2.8 kpc is assumed. The EM is shown in the same units as in Table 4. The solid lines indicate two conditions, $n_e v_{\text{sh}} = \text{const.}$ (green) and $n_e v_{\text{sh}}^2 = \text{const.}$ (blue).

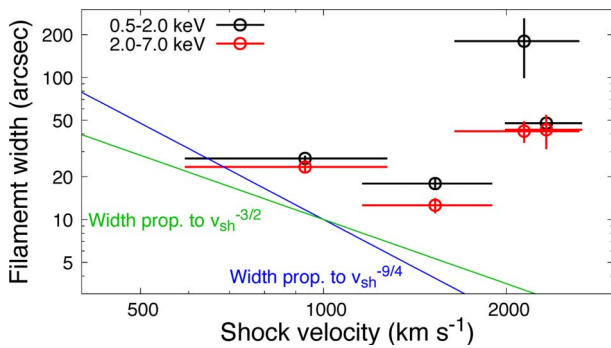


Figure 16. Plots of the filament width (w) against the shock velocity (v_{sh} ; proper motion velocity is substituted). A distance of 2.8 kpc is assumed. The solid lines indicate two functions, $w \propto v_{\text{sh}}^{-3/2}$ (green) and $w \propto v_{\text{sh}}^{-9/4}$ (blue).

(Figure 14(b-1)) can be understood as a more enhanced nonthermal particle density in higher-density regions. The shock–cloud interaction leads highly spatially inhomogeneous magnetic fields, and so the power-law parameters show large scatter even at similar shock velocities (Figure 14(a)). However, interestingly, the plasma density seems to remain a good tracer of the modification of the acceleration conditions even after the interaction (Figure 14(b)).

The reason for the apparent inconsistency of our estimates of the magnetic field strengths and shock velocities with the Bell instability (Figure 16) is understandable if the magnetic turbulence induced by the shock–cloud interaction determines local acceleration activity. Note that, according to a comparison with other SNRs, the amplification level of the base magnetic field over the whole remnant seems to be controlled by the Bell instability (Vink 2006; Helder et al. 2012). Thus, it is suggested that the local magnetic turbulence levels $\delta B/B$ are of great importance for understanding the local acceleration conditions.

In Figure 14(b), the tendency of the inner nonthermal-dominated filaments (SW6, SW7, and SW10) differs from that of the outer filaments. If we assume that the outer filaments are newly interacting with dense gas and the inner ones are still in the wind-blown bubble, our results may suggest that the cavity region has different acceleration conditions from the interacting regions, which is naturally expected.

As a conclusion, our findings suggest that the physics of acceleration at the outer filaments of the RCW 86 SW region is governed by the ambient density, and not or only weakly by the

shock velocity and shock obliquity. We find that the shock–cloud interaction scenario can explain the measurements consistently, although not yet in a quantitative manner. Radio observations with high angular resolutions (e.g., Atacama Large Millimeter/submillimeter Array) will greatly help test our scenario.

5. Conclusion

In this work, we studied the X-ray proper motions and spectral properties of the RCW 86 SW region. The proper motion velocities were found to be $\sim 300\text{--}2000 \text{ km s}^{-1}$ at a distance of 2.8 kpc. We found two inward-moving filaments. They were found to be nonthermal-dominated, and spectral softening was seen in the downstream direction, which confirmed their inward movements. It is likely that they are reflected shocks rather than reverse shocks. Based on the X-ray spectroscopy, we evaluated thermal parameters such as the ambient density and temperature, and nonthermal parameters such as the power-law flux and index. Also, based on the decrease in flux of several nonthermal filaments, we were able to estimate the magnetic field amplitudes of $\sim 30\text{--}100 \mu\text{G}$.

Gathering the proper motion and X-ray properties, we then studied the parameter correlations. We found that, at the outer thermal-dominated filaments, the nonthermal parameters were correlated with the ambient density as (power-law flux) $\propto n_e^{1.0 \pm 0.2}$ and (power-law index) $\propto n_e^{0.38 \pm 0.10}$, and not or only weakly correlated with the shock velocity and shock obliquity. These indicate harder and fainter synchrotron emission for lower-density regions. As an interpretation of the measured physical parameters, we propose the shock–cloud interaction scenario, where the locally enhanced magnetic turbulence levels ($\delta B/B$) have a great influence on the local acceleration conditions. The inner nonthermal-dominated filaments showed a different tendency from that of the outer filaments, which is understandable if the inner ones are still in the wind-blown bubble and have different acceleration conditions.

We appreciate helpful suggestions provided by the anonymous referee, which have improved the paper significantly. We are grateful to K. Kawabata for providing the software to extract the starlight polarization data. This work was partially supported by JSPS grant Nos. 19J11069 and 21J00031 (H.S.), 20H00174, 21H01121 (S.K.), 19H01936, 21H04493 (T.T.), and 20H01944 (T.I.). F.F. was supported, in part, by NASA through Chandra Theory Award Number TM0–21001X, issued by the Chandra X-ray Observatory Center, which is operated by the Smithsonian Astrophysical Observatory for and on behalf of NASA under contract NAS8-03060.

Facilities: Chandra.

Software: HEASoft (v6.20; HEASARC 2014), CIAO (v4.11; Fruscione et al. 2006), mkacispack (v2021-07-15; Suzuki et al. 2021).

Appendix A Flux Profiles across the Filaments

The X-ray flux profiles of individual filaments in 2001 and 2013 are shown in Figures 17 and 18. The radial ranges indicated with the dotted lines are used to calculate the proper motion velocities.

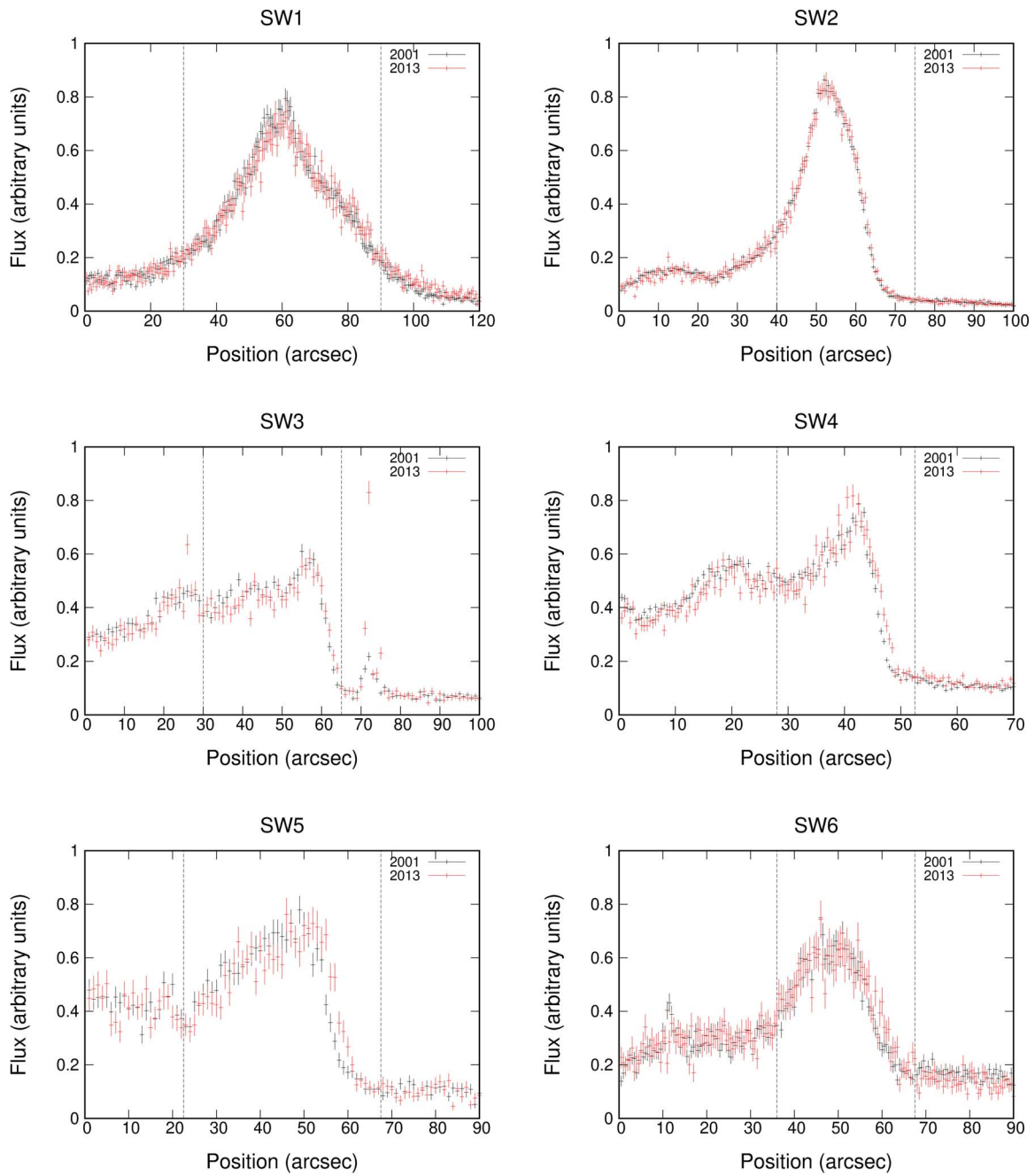


Figure 17. Flux profiles of the regions SW1–SW6. The black and red crosses represent the data taken in 2001 and 2013, respectively. The positive directions of positions correspond to the directions of the arrows shown in Figure 1. The displayed flux ranges are different for different panels. The vertical dashed lines represent the ranges used for proper motion measurement.

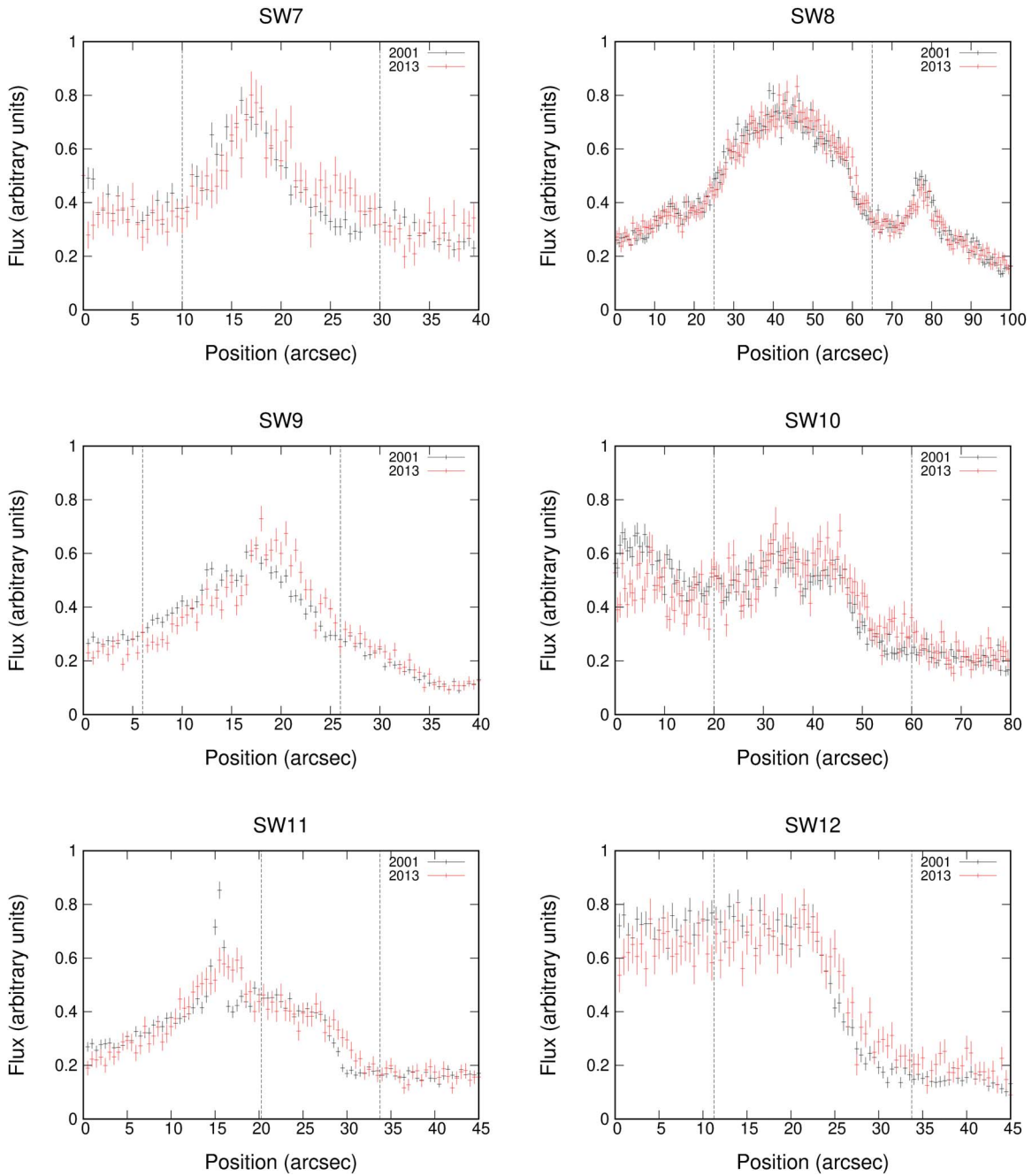


Figure 18. Flux profiles of the regions SW7–SW12. The same convention for the plots is used as in Figure 17.

Appendix B Other Parameter Correlations

In order to investigate the dependence of the nonthermal parameters on the shock obliquity, we first estimate the magnetic field directions as follows. We use the starlight polarization data compiled by Heiles (2000). This database includes the polarization properties of $\sim 10,000$ stars with their positions and distances. We extract the data for the stars in a $20^\circ \times 20^\circ$ square region centered on $(l, b) = (315^\circ.4015, -2^\circ.31664)$ at distances of 2–4 kpc. The resultant magnetic field directions around RCW 86, which directly correspond to the directions of starlight polarization, are presented in

Figure 19. The directions are found to be nearly parallel to the Galactic plane. We then calculate the shock obliquity of each filament assuming that the filaments have been moving directly away from the explosion center estimated in Section 4.3 (case (a)). The plots of the power-law parameters over the shock obliquity are presented in Figure 20. No clear correlations are found. Instead of assuming the simple filament motion away from the explosion center, we have also assumed that the shock normal directly corresponds to the direction of motion we defined in Figure 1 (case (b)). This assumption also results in similar plots (Figure 20), without significant correlations.

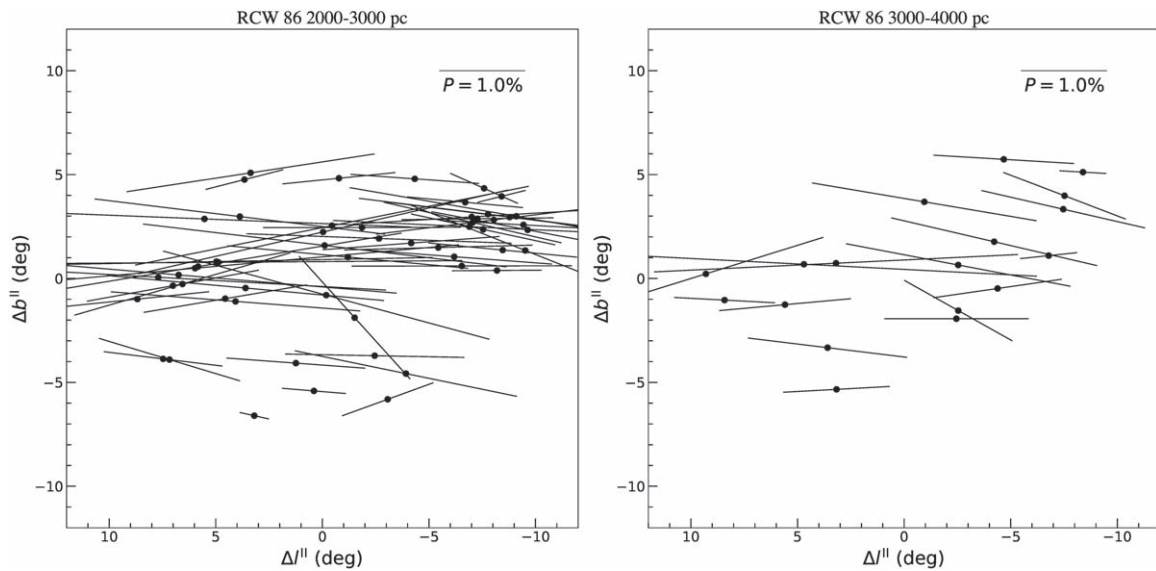


Figure 19. Magnetic field directions estimated at the stars around the RCW 86 region. Δl^{II} , Δb^{II} , and P indicate the Galactic longitude and latitude with respect to the coordinates $(l, b) = (315^{\circ}4015, -2^{\circ}31664)$, and polarization degree, respectively. Left and right panels show the estimates for distances of 2–3 kpc and 3–4 kpc, respectively.

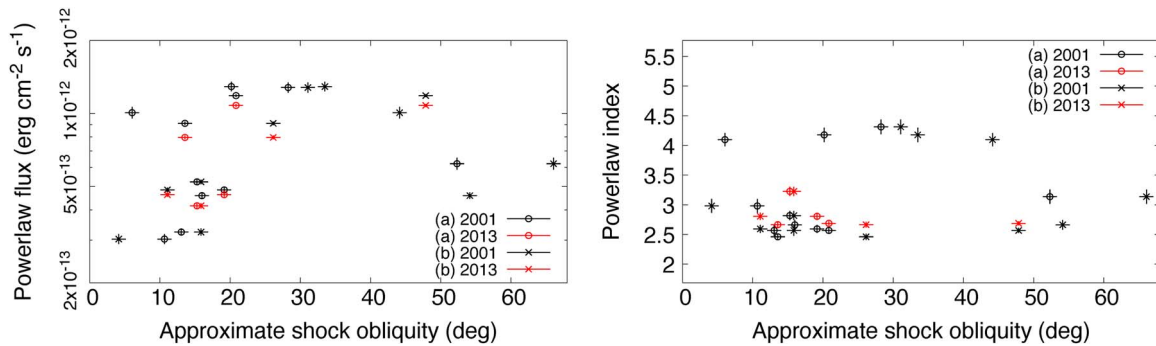


Figure 20. Plots of the power-law flux and index against the shock obliquity. As a proxy for the shock obliquity, we assume two cases: we use the angle made by the Galactic plane and the vector connecting the filament position and geometric center of RCW 86 (case (a)), and the angle made by the Galactic plane and the direction of motion of the filament defined in Figure 1 (case (b)). For the shock obliquity, a typical error of 1° is assigned to all the regions.

ORCID iDs

Hiromasa Suzuki <https://orcid.org/0000-0002-8152-6172>
 Satoru Katsuda <https://orcid.org/0000-0002-1104-7205>
 Takaaki Tanaka <https://orcid.org/0000-0002-4383-0368>
 Tsuyoshi Inoue <https://orcid.org/0000-0002-7935-8771>
 Federico Fraschetti <https://orcid.org/0000-0002-5456-4771>

References

- Allen, C., Jerius, D. H., & Gaetz, T. J. 2004, *Proc. SPIE*, 5165, 423
 Amato, E., & Blasi, P. 2006, *MNRAS*, 371, 1251
 Arnaud, K. A. 1996, in ASP Conf. Ser. 101, *Astronomical Data Analysis Software and Systems V*, ed. G. H. Jacoby & J. Barnes (San Francisco, CA: ASP), 17
 Bamba, A., Koyama, K., & Tomida, H. 2000, *PASJ*, 52, 1157
 Bamba, A., Yamazaki, R., Yoshida, T., Terasawa, T., & Koyama, K. 2005, *ApJ*, 621, 793
 Bell, A. R. 2004, *MNRAS*, 353, 550
 Dickel, J. R., Strom, R. G., & Milne, D. K. 2001, *ApJ*, 546, 447
 Fraschetti, F. 2013, *ApJ*, 770, 84
 Fraschetti, F., Katsuda, S., Sato, T., Jokipii, J. R., & Giacalone, J. 2018, *PhRvL*, 120, 251101
 Fruscione, A., McDowell, J. C., Allen, G. E., et al. 2006, *Proc. SPIE*, 6270, 586
 Garmire, G. P. 1997, AAS Meeting, 190, 34.04
 Giacalone, J., & Jokipii, J. R. 2007, *ApJL*, 663, L41
 Green, D. A., & Stephenson, F. R. 2003, in *Supernovae and Gamma-Ray Bursters*, ed. K. Weiler, Vol. 598 (Berlin: Springer), 7
 HEASARC 2014, HEASoft: Unified Release of FTOOLS and XANADU, Astrophysics Source Code Library, ascl:1408.004
 Heiles, C. 2000, *AJ*, 119, 923
 Helder, E. A., Vink, J., Bykov, A. M., et al. 2012, *SSRv*, 173, 369
 HI4PI Collaboration, Ben Bekhti, N., Flöer, L., et al. 2016, *A&A*, 594, A116
 Hickox, R. C., & Markevitch, M. 2006, *ApJ*, 645, 95
 Inoue, T., Yamazaki, R., Inutsuka, S.-i., & Fukui, Y. 2012, *ApJ*, 744, 71
 Katsuda, S., Petre, R., Mori, K., et al. 2010, *ApJ*, 723, 383
 Kishishita, T., Hiraga, J., & Uchiyama, Y. 2013, *A&A*, 551, A132
 Kuntz, K. D., & Snowden, S. L. 2000, *ApJ*, 543, 195
 Kushino, A., Ishisaki, Y., Morita, U., et al. 2002, *PASJ*, 54, 327
 Masui, K., Mitsuda, K., Yamasaki, N. Y., et al. 2009, *PASJ*, 61, S115
 Pohl, M., Yan, H., & Lazarian, A. 2005, *ApJL*, 626, L101
 Ressler, S. M., Katsuda, S., Reynolds, S. P., et al. 2014, *ApJ*, 790, 85
 Reynolds, S. P. 2008, *ARA&A*, 46, 89
 Reynolds, S. P., Williams, B. J., Borkowski, K. J., & Long, K. S. 2021, *ApJ*, 917, 55
 Rho, J., Dyer, K. K., Borkowski, K. J., & Reynolds, S. P. 2002, *ApJ*, 581, 1116
 Rosado, M., Ambrocio-Cruz, P., Le Coarer, E., & Marcelin, M. 1996, *A&A*, 315, 243
 Sano, H., Fukuda, T., Yoshiike, S., et al. 2015, *ApJ*, 799, 175
 Sano, H., Reynoso, E. M., Mitsuishi, I., et al. 2017, *JHEAp*, 15, 1
 Sano, H., Rowell, G., Reynoso, E. M., et al. 2019, *ApJ*, 876, 37
 Sano, H., Tanaka, T., Torii, K., et al. 2013, *ApJ*, 778, 59
 Sato, T., Katsuda, S., Morii, M., et al. 2018, *ApJ*, 853, 46

- Smith, R. C. 1997, *AJ*, **114**, 2664
- Snowden, S. L., Plucinsky, P. P., Briel, U., Hasinger, G., & Pfeffermann, E. 1992, *ApJ*, **393**, 819
- Stephenson, F. R., & Green, D. A. 2002, *Historical Supernovae and their Remnants*, Vol. 5 (Oxford: Clarendon)
- Suzuki, H., Bamba, A., Yamazaki, R., & Ohira, Y. 2020, *PASJ*, **72**, 72
- Suzuki, H., Bamba, A., Yamazaki, R., & Ohira, Y. 2022, *ApJ*, **924**, 45
- Suzuki, H., Plucinsky, P. P., Gaetz, T. J., & Bamba, A. 2021, *A&A*, **655**, A116
- Tran, A., Williams, B. J., Petre, R., Ressler, S. M., & Reynolds, S. P. 2015, *ApJ*, **812**, 101
- Truelove, J. K., & McKee, C. F. 1999, *ApJS*, **120**, 299
- Tsubone, Y., Sawada, M., Bamba, A., Katsuda, S., & Vink, J. 2017, *ApJ*, **835**, 34
- Tsuji, N., Uchiyama, Y., Aharonian, F., et al. 2019, *ApJ*, **877**, 96
- Tsuji, N., Uchiyama, Y., Khangulyan, D., & Aharonian, F. 2021, *ApJ*, **907**, 117
- Uchiyama, Y., Aharonian, F. A., Tanaka, T., Takahashi, T., & Maeda, Y. 2007, *Natur*, **449**, 576
- Vink, J. 2006, in *ESA Special Publication*, 604, *The X-ray Universe 2005* (ESA SP-604), ed. A. Wilson
- Vink, J. 2017, in *Handbook of Supernovae*, ed. A. W. Alsabti & P. Murdin (Cham: Springer), 2063
- Vink, J., Bleeker, J., van der Heyden, K., et al. 2006, *ApJL*, **648**, L33
- Völk, H. J., Berezhko, E. G., & Ksenofontov, L. T. 2005, *A&A*, **433**, 229
- Williams, B. J., Blair, W. P., Blondin, J. M., et al. 2011, *ApJ*, **741**, 96
- Yamaguchi, H., Katsuda, S., Castro, D., et al. 2016, *ApJL*, **820**, L3
- Yamaguchi, H., Koyama, K., & Uchida, H. 2011, *PASJ*, **63**, S837
- Yamazaki, R., Ohira, Y., Sawada, M., & Bamba, A. 2014, *RAA*, **14**, 165
- Yoshino, T., Mitsuda, K., Yamasaki, N. Y., et al. 2009, *PASJ*, **61**, 805
- Yuan, Q., Huang, X., Liu, S., & Zhang, B. 2014, *ApJL*, **785**, L22
- Zeng, H., Xin, Y., & Liu, S. 2019, *ApJ*, **874**, 50
- Zirakashvili, V. N., & Aharonian, F. 2007, *A&A*, **465**, 695